Water Air Soil Pollut (2014) 225:2195
DOI 10.1007/s11270-014-2195-3

Nanoscale Zero-Valent Iron Supported on Biochar: Characterization and Reactivity for Degradation of Acid Orange 7 from Aqueous Solution

Guixiang Quan · Wenji Sun · Jinlong Yan · Yeqing Lan

Received: 4 August 2014 / Accepted: 16 October 2014 / Published online: 31 October 2014

Abstract The nanoscale zero-valent iron supported on biochar (B-nZVI) was prepared by liquid-phase reduction method and used for the removal of acid orange 7 (AO_7). The structure of composited B-nZVI was characterized by transmission electron microscopy, scanning electron microscopy, X-ray diffraction analysis, X-ray photoelectron spectroscopy, and Brunauer-Emmett-Teller surface area analysis. nZVI was well dispersed on the surface of biochar with a specific surface area 52.21 m^2/g, and no obvious aggregation was observed. Batch experiments demonstrated that the degradation of AO_7 (20 mg/L) by B-nZVI (2 g/L) at initial pH 2 reached 98.3 % within 10 min. There was a good linearity (r^2=0.99) between k_{obs} and B-nZVI dosage. The reductive cleavage of the azo group in AO_7 to amino group may be the dominant stage. This study demonstrated that B-nZVI has the potential to be a promising material for the removal of azo dyes.

Keywords Nanoscale zero-valent iron · Biochar · Synthesis and characterization · Acid orange 7 · Removal

1 Introduction

Azo dyes (−N=N– unit as the chromophore) are widely utilized in leather, papermaking, printing, and textile dyeing because of their chemical stability and versatility (Brown 1987). These azo dyes are also known to be largely non-biodegradable in aerobic conditions and to be reduced to more hazardous intermediates in anaerobic conditions (Park and Choi 2003). Therefore, it is necessary to find novel and efficient approaches to treating the industrial wastewater containing azo dyes.

Up to now, the removal of azo dyes in wastewater mainly includes physical, chemical, biological methods or combination of various methods (Forgacs et al. 2004), such as electrochemical treatment (Martínez-Huitle and Brillas 2009), ozonation (Szpyrkowicz et al. 2001), photocatalysis (Han et al. 2009), Fenton or Fenton-like reagents (Malik and Saha 2003). Nevertheless, many of these methods are often ineffective for the destruction of azo dyes and meanwhile result in large quantities of solid wastes or other environmental problems during the treatment processes (Azam and Hamid 2006). Recently, an approach based on zero-valent iron (ZVI) to the degradation of organic

Electronic supplementary material The online version of this article (doi:10.1007/s11270-014-2195-3) contains supplementary material, which is available to authorized users.

G. Quan · Y. Lan (✉)
College of Sciences, Nanjing Agricultural University, Nanjing 210095, People's Republic of China
e-mail: lanyq102@njau.edu.cn

G. Quan · W. Sun · J. Yan
School of Environmental Science and Engineering, Yancheng Institute of Technology, Yancheng 224051, People's Republic of China

compounds and the remediation of groundwater attracts wide attention (Liu et al. 2007). High decolorization rates have been achieved in the reactions of nine azo dyes with particle Fe^0 (Nam and Tratnyek 2000). ZVI together with activate molecular oxygen in air produces reactive oxygen species containing superoxide radical, hydroxyl radical, and hydrogen peroxide, which further oxidize organic contaminants (Wang et al. 2014). Compared with ZVI, nanoscale zero-valent iron (nZVI) possesses a larger specific surface area (SSA) and higher reactivity and degrades many organic targets more effectively (Wang and Zhang 1997). However, nZVI particles can easily agglomerate into larger ones and be oxidized by non-target compounds because of their high surface energy and intrinsic magnetic interaction (Phenrat et al. 2007). Several techniques have been developed for enhancing the stability of nZVI. For instance, nZVI particles are supported on solids (He and Zhao 2005; Quan et al. 2014) or entrapped in polymers (Liu et al. 2010).

Biochar is stable recalcitrant and produced by pyrolysis of biomass under low (preferably zero) oxygen concentration (Zhou et al. 2014). Various types of the carbon-rich biomass including agricultural wastes or residues are utilized to produce biochar through the pyrolysis process (Chen et al. 2011; Cao et al. 2013). Biochar has already been put into use as a mechanical support to disperse and stabilize engineered nanoparticles due to its porous structure and large specific surface area SSA (Yao et al. 2013). It is premised that biochar as a support is conducive to transferring organic targets to the surface of nZVI owing to the adsorption of targets by biochar and facilitating the degradation of contaminants. However, little information is available on supporting nZVI on the surface of biochar. To the best of our knowledge, there are still no reports on the degradation of azo dyes by biochar-supported nanoparticle zero-valent iron (B-nZVI), and the degradation mechanism is not understood.

In this study, B-nZVI was synthesized and characterized, and the feasibility of the removal of AO_7 by B-nZVI was thoroughly examined. The effects of various parameters including initial pH, B-nZVI dosage, and initial concentration of AO_7 on the removal efficiency were also assessed. In addition, the kinetics was investigated by fitting the experimental data with a kinetic model and the rate constants were then calculated. Based on the observation of UV curves in the degradation process, a potential degradation pathway was proposed.

2 Materials and Methods

2.1 Materials

Biochar was purchased from Zhongke Anda Science and Technology Ltd, Shanghai China, which was produced by heating bush branch at 350–550 °C under limited oxygen supply. The cation exchange capacity (CEC) and SSA of biochar are 14.57 mmol/100 g and 4.22 m^2/g, respectively. The pretreatment of biochar was as follows: after biochar was ground into a size of 200-mesh, 10.0 g of the collected biochar was immersed in 250-mL 0.05 mol/L H_2SO_4 at 45 °C for 48 h under mechanical string at 300 rpm, washed with distilled water, and then dried (Chen, et al. 2007). Potassium borohydride (KBH_4, 99.9 %), ferrous sulfate heptahydrate ($FeSO_4 \cdot 7H_2O$, 99 %), and AO_7 (99.9 %) were obtained from Sigma–Aldrich. Absolute ethanol, sulfuric acid, and sodium hydroxide were purchased from Sinopharm Chemical Reagent Company and used without further purification.

2.2 Preparation of B-nZVI

B-nZVI was prepared using a conventional liquid-phase method via the reduction of ferrous iron by borohydride with biochar as a support material. In a typical procedure, 2.0-g preprocessed biochar was firstly suspended in 60-mL 1.0 mol/L $FeSO_4$ and stirred for 2 h to adsorb Fe^{2+} onto biochar. Then, 90-mL ethanol (50 %) was added, and 100-mL 0.4 mol/L of freshly prepared KBH_4 was introduced drop-wise to the suspension and kept continuous stirring for 2 h. The whole preparation process described above was performed under nitrogen atmosphere to avoid oxidization.

The reaction can be expressed as

$$Fe^{2+} + 2\,BH_4^- + 6\,H_2O \rightarrow Fe^0 + 2\,B(OH)_3 + 7\,H_2\uparrow \quad (1)$$

Subsequently, the suspension was centrifuged and washed several times with absolute ethanol instead of water to avoid the immediate oxidation of B-nZVI (Shi et al. 2011), and then the precipitates were put in a vacuum drying oven at 60 °C for 8 h. Finally, the products were stored in glove box prior to use.

2.3 Characterization

2.3.1 Transmission Electron Microscopy (TEM)

TEM images were taken with a JEM-2100 (JEOL Electronics Co., Tokyo Japan) using an accelerating voltage of 200 kV. The samples were put on 300-mesh Cu TEM grids with a carbon film and dried in the anaerobic condition for 24 h.

2.3.2 Scanning Electron Microscopy (SEM)

The morphological analysis of the samples was performed using a field emission scanning electron microscope (S4800, Hitachi Co., Japan) with an EX-250 energy dispersive X-ray analyzer system, and the samples were coated with carbon.

2.3.3 Specific Surface Area (SSA)

Nitrogen sorption isotherms were analyzed with an ASAP 2020 (Micromeritics, USA) at 77 K. Before the measurements, all samples were degassed 2 h at 573 K in a vacuum line. The Brunauer-Emmett-Teller (BET) method was utilized to calculate SSA. The pore volume and size distribution were derived from the desorption branches of the isotherms using the Barrett–Joyner–Halenda (BJH) model.

2.3.4 X-ray Photoelectron Spectroscopy (XPS)

To investigate the change of chemical binding of iron species on the surface of B-nZVI and the surface chemical composition, XPS was conducted on a RBD upgraded Thermo ESCALAB 250 system with an Al Kα X-ray (1486.6 eV) with a source power of 150 W. The samples were carefully packed on XPS sampling template under the anaerobic condition to avoid surface oxidation. Raw spectra were smoothed before being fitted using a Shirley base line and a Gaussian-Lorentzian shape peak. Narrow scanned spectra were used to obtain the chemical state information on iron (kinetic energy Ek 546 eV) and oxygen (Ek 724 eV).

2.3.5 X-ray Diffraction Analysis (XRD)

The samples were also characterized by XRD. Standard X-ray powder patterns were recorded on a vertical X-ray diffractometer (X'Pert-Pro MPD, Philips, the Netherlands) between 5° and 90° (2θ), using Cu Kα radiation (λ=0.15406 nm) generated at 40 kV and 40 mA. The crystalline phases were identified by matching with the JCPDS (Joint Committee on Powder Diffraction Standards) files.

2.4 AO_7 Degradation by B-nZVI

Batch experiments for the removal of AO_7 in aqueous solutions were performed in 250-mL conical flasks with 100 mL of 20 mg/L AO_7. An appropriate dosage of B-nZVI was added to the flask, which was immediately sealed, then put into a vapor bath at a constant temperature of 25 °C and vibrated at a speed of 200 rpm for 2 h. Afterwards, an aliquot of supernatant was sampled at regular intervals and filtered through 0.2-μm membrane filter (millipore) for AO_7 analysis using a UV–vis spectrophotometer (T6, Puxi Company, Beijing, China) at 484-nm wavelength. After reaction, particulate materials were collected by centrifugation and separation from the supernatant. The collected samples were vacuum-dried and analyzed by SEM, BET, and XRD.

The effect of initial pH on AO_7 removal efficiency was conducted in the range of 2 to 9 adjusted by diluted HCl or NaOH. The value of pH was measured on a pH meter (pHS-3B, Shanghai, China). Each experiment was run in triplicate and the mean values were reported.

2.5 Kinetic Study

To investigate the reaction rate constants, a pseudo-first-order kinetics model was adopted in this study. The equation with respect to the concentration of AO_7 is expressed as

$$v = -\mathrm{d}c_{\mathrm{AO7}}/\mathrm{d}t = k_{\mathrm{obs}}c_{\mathrm{AO7}} \tag{2}$$

where k_{obs} is the observed first-order reaction rate constant, which is obtained through the slope of the regression lines by plotting a natural log graph with respect to AO_7 concentration and reaction time according to the following equation:

$$\ln\left[c_{0(\mathrm{AO7})}/c_{\mathrm{e(AO7)}}\right] = k_{\mathrm{obs}}t \tag{3}$$

where c_0 and c_e represent AO_7 concentrations at the initial and t time, respectively.

3 Results and Discussion

3.1 Characterization of B-nZVI

3.1.1 TEM

The TEM images of B-nZVI are shown in Fig. 1. B-nZVI was mainly comprised of two phases, nZVI with diameter around 20–60 nm and biochar (Fig. 1). In addition, the images demonstrated a good dispersion of individual nZVI adhering on the surface of biochar without notable aggregation and the irregular shapes of biochar with mesoporous structures.

3.1.2 SEM and EDX

The SEM images of the biochar and B-nZVI before and after the reaction with AO_7 are shown in Fig. 2. The surface of biochar treated with diluted acid was smooth, and the vasculars of various diameters formed tracheid cells (Fig. 2a), providing a high internal surface and high adsorption capacity as previously reported (Xu et al. 2014). nZVI was well dispersed on the surface of biochar without obvious aggregation, and the sizes of the particles ranged from several to hundred nanometers (Fig. 2b and c). A quite different appearance of B-nZVI after the reaction with AO_7 was observed (Fig. 2d), implying that nZVI on biochar may be consumed and the twisting structure of biochar almost completely collapsed.

The EDX mapping and element analysis of B-nZVI are presented in Fig. 3. A weak peak from Fe was observed in the EDX spectrum of the selected sample area (Fig. 3a), which confirmed the presence of Fe elements. In order to verify the uniformity of nanocomposites, an element mapping analysis is illustrated in Fig. 3b to d, and the bright spots indicated the presence of the elements C, Fe, and O. Moreover, the mapping shape of Fe element implied that nZVI may be uniformly dispersed on the surface of biochar.

3.1.3 BET

The pore structure and the SSA of samples were determined by N_2 adsorption-desorption. As observed in Fig. 4, the samples displayed typical IUPAC type-IV adsorption isotherm patterns with a hysteresis loop appearing in a wide pressure range at a relatively high pressure (P/P_0=0.5–0.95). The SSA of biochar treated with water and diluted acid was determined to be 4.32 and 8.51 m^2/g, respectively. For B-nZVI before and after the reaction with AO_7, however, they were 52.21 and 92.75 m^2/g, respectively. The SSA of biochar obtained in this study was very low, which was perhaps related to the measuring method with BET. The liquid N_2 adsorption BET method (77 K) is commonly used. But it may be inaccurate for materials that contain micropores (<1.5-nm pore diameter) since N_2 may be kinetically limited in its diffusion into small pores at low temperatures. Yao et al. (2011) reported that the N_2 surface area of sugar beet tailing biochar (STC) was very low (2.6 m^2/g), but the CO_2 surface area of STC was above (351 m^2/g). Zhang et al. (2012) also found that the SSA of peanut shell biochar (PS) and pine wood biochar (PW) determined by CO_2 were much larger (346.5 and 432.6 m^2/g, respectively) than those of PS (18.9 m^2/g) and PW (2.8 m^2/g) determined by N_2.

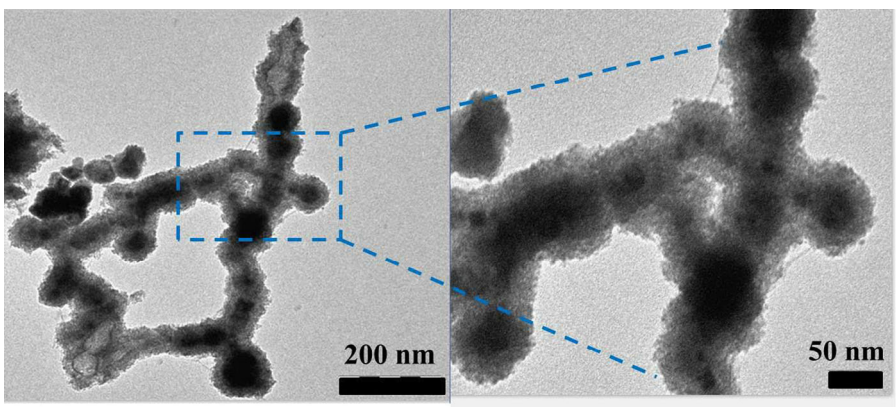

Fig. 1 TEM images of the nZVI grafted on biochar

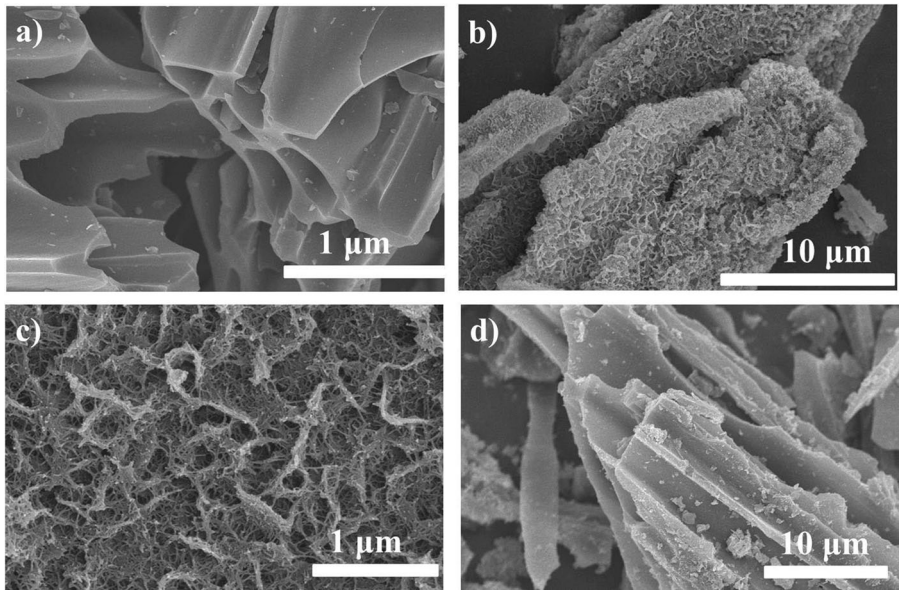

Fig. 2 SEM images of samples for biochar treated with diluted acid (**a**), nZVI grafted on the biochar of different magnification times (**b**, **c**), and nZVI grafted on the biochar after the reaction with AO_7 (**d**)

It was found that the SSA of B-nZVI was larger than that of biochar. This was attributed to the interlayer-bound small iron pillars, which could prop the micropores and then increased the SSA. Moreover, nZVI with sizes larger than the diameter of micropores coated on the external surfaces of the matrix also resulted in an increase of SSA (Luo et al. 2013). Nevertheless, it is speculated that the disappearance of nZVI in the

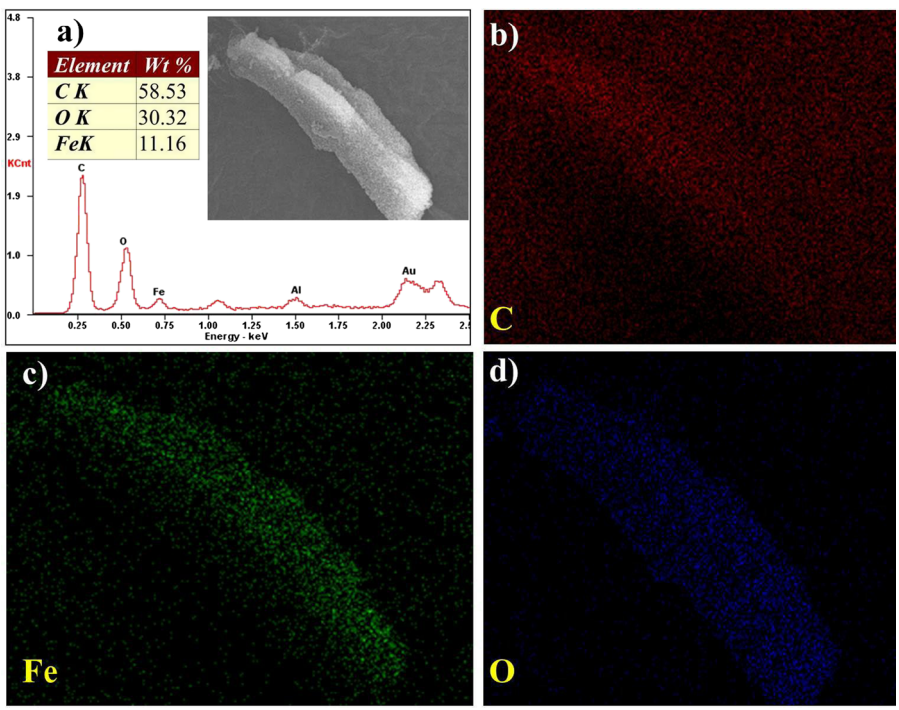

Fig. 3 EDX mapping and element analysis on B-nZVI. SEM image and EDX spectrum of selected area (**a**), C element distribution (**b**), Fe element distribution (**c**), and O element distribution (**d**)

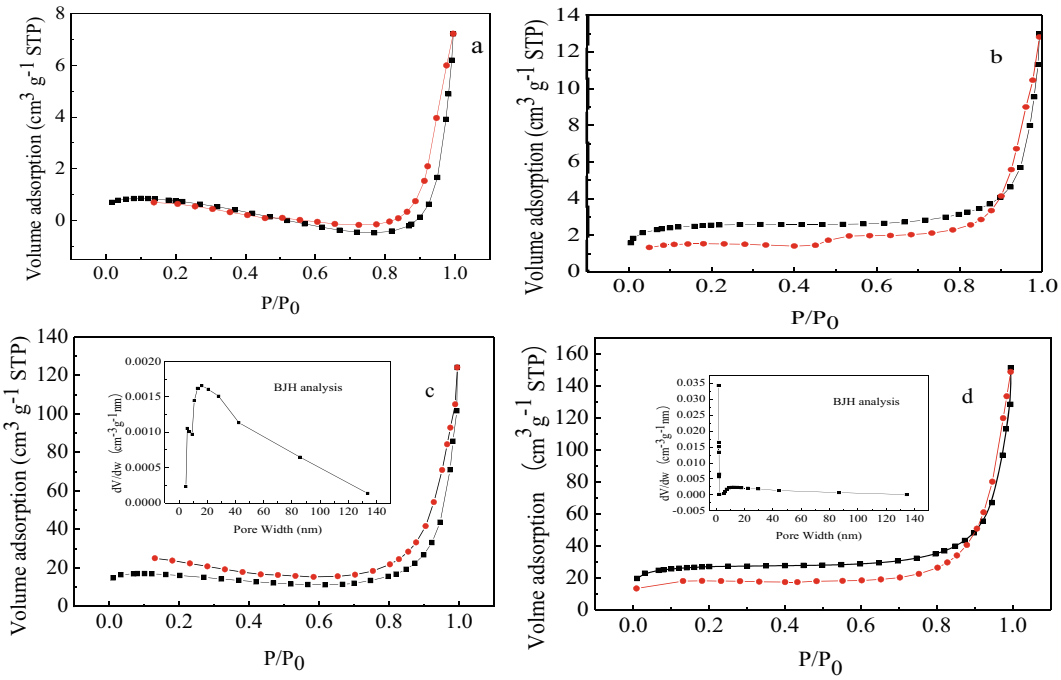

Fig. 4 Nitrogen sorption isotherms and pore size distribution (inset) of biochar. Biochar treated with water (**a**), biochar treated with diluted acid (**b**), nZVI grafted on the biochar (**c**), and nZVI grafted on the biochar after reaction with AO_7 (**d**)

micropores during the reaction can lead to a larger SSA of B-nZVI. Therefore, the SSA of B-nZVI after the reaction was obviously enhanced.

3.1.4 XPS

Primary elements in the B-nZVI included C, O, Si, and Fe (see Fig. S1a.). The binding energies of these elements were at C 1s 284.8 ev, O 1s 532.1 ev, and Fe 2p 707.4 ev, and the percentages were 57.97, 32.68, and 9.17 %, respectively. The analysis of iron content was similar to the EDX mapping. The detail in Fe 2p orbit is presented in Fig. S1b, demonstrating Fe 2p levels were different. The photoelectron peaks at 707.4 and 720.8 ev corresponded to the binding energies of Fe 2p 3/2 and Fe 2p 1/2, respectively. A strong peak at 707.4 ev corresponded to zero-valent iron (Fe^0 $2p_{3/2}$) (Liu et al. 2010). Thus, the results shown in Fig. S1b implied that the B-nZVI may be partially oxidized during the preparation or characterization process.

3.1.5 XRD

XRD images are shown in Fig. S2. A weak peak appeared at 2θ=44.6° in B-nZVI (Fig. S2b), which was assigned to the 110 plane reflections of the ZVI with a body centered cubic structure (Hoch et al. 2008). Other peaks in 2θ=22–30° were also observed for biochar, which were assigned to the amorphous carbonaceous structure of organic matrix. But after the reaction with AO_7 (Fig. S2c), all the peaks became weak, which suggested that the crystal structure of biochar may not be well kept. The peak of Fe in Fig. S2c disappeared due to the oxidization of nZVI to Fe^{2+} or Fe^{3+}.

3.2 Degradation of AO_7 by B-nZVI

3.2.1 Effect of Initial pH on the Removal of AO_7

The degradation of azo dye by ZVI is greatly affected by pH due to the formation of $Fe(OH)_3$ in a high pH solution, which coats on the surface of ZVI particles and reduces the activity of ZVI (Huang et al. 1998). In this study, therefore, the effects of initial pH on the removal of AO_7 by biochar treated with dilute acid and B-nZVI were investigated and the results are illustrated in Fig. 5. It was found that in the presence of biochar alone, the removal rate of AO_7 was only approximately 36.5 % at pH 2.0 and 12.5 % at pH 9.0 after equilibrium due to adsorption. However, B-nZVI at the

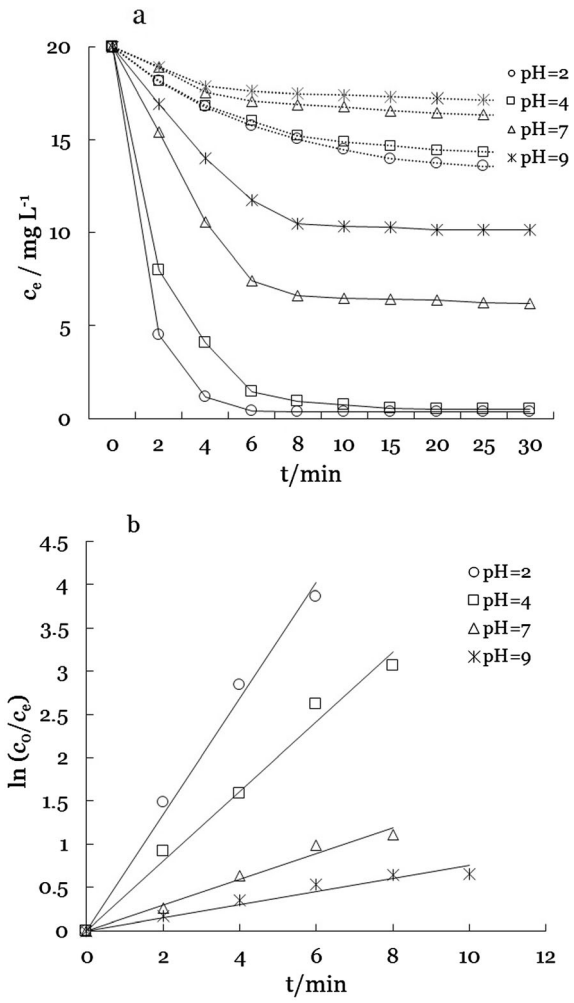

Fig. 5 Effect of inital pH value on the removal of AO_7 by biochar and B-nZVI at room temperature. *Dashed lines* indicate biochar, *solid lines* indicate B-nZVI; c_0=20 mg/L; $c_{biochar}$=2.0 g/L, $c_{B\text{-}nZVI}$=2.0 g/L; stirring at 200 rpm

same dosage (2 g/L) exhibited a high potential for AO_7 degradation, and the removal efficiency reached approximately 98.3 % at pH 2.0 and 48 % at pH 9.0. On the other hand, the microparticles of Fe^0 exhibited a weak reductive role in AO_7 degradation since the rapidly produced film of $Fe(OH)_3$ blocked the access of target contaminants to active sites of ZVI (data not shown). Therefore, it is concluded that there was a synergistic effect existing between Fe^0 and substrate biochar, in which biochar accelerated AO_7 molecules to transfer onto the surface of nZVI due to adsorption and then enhanced the reductive degradation of AO_7.

Obviously, the degradation rate and removal efficiency of AO_7 by B-nZVI rapidly decreased with an

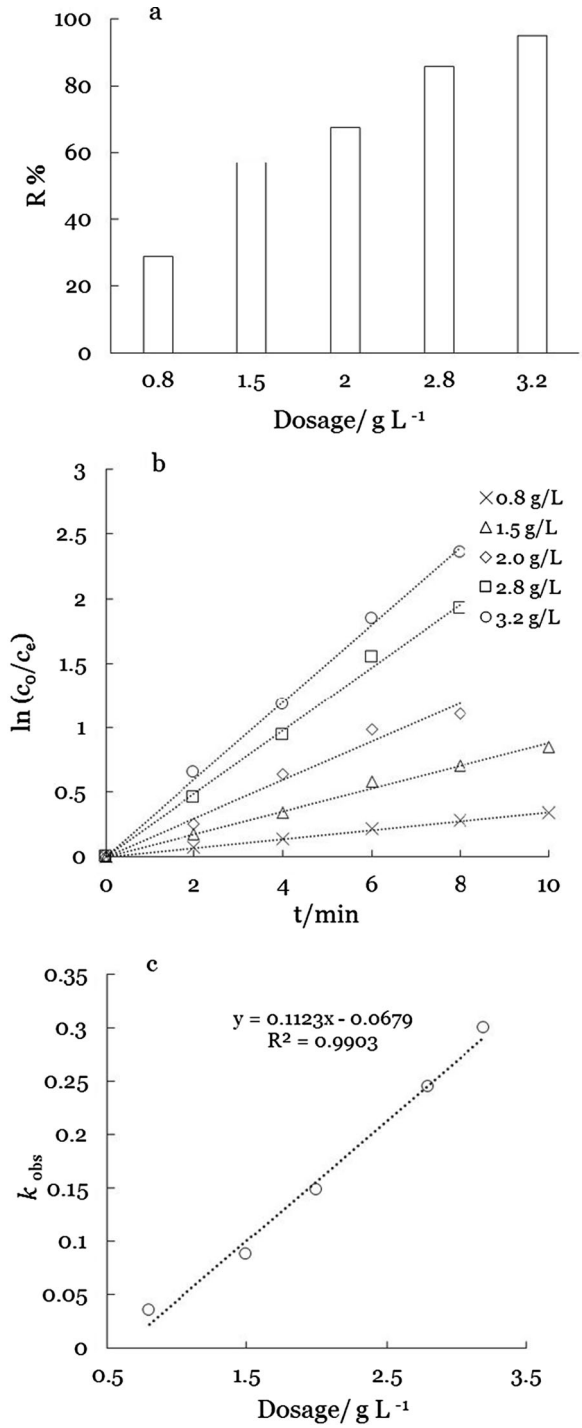

Fig. 6 Effect of dosage on the removal efficiency at 10 min: removal efficiency (**a**), the kinetics curves (**b**), and the relationship between k_{obs} and dosage of B-nZVI (**c**). c_0=20 mg/L; $pH_{initial}$= 7.0; and stirring at 200 rpm

increase of initial pH. It is noted that the plotting of $\ln[c_{0(AO7)}/c_{e(AO7)}]$ against reaction time (t< 10 min)

displayed a good linearity (r^2>0.944), suggesting that the degradation of AO_7 by B-nZVI may obey pseudo-first-order reaction kinetics. The values of k_{obs} at pH 2.0, 4.0, 7.0, and 9.0 were 0.67, 0.40, 0.15, and 0.076 min^{-1}, respectively. k_{obs} at pH 2.0 was eight times as much as that of pH 9. According to Nernst equation, the reduction ability of Fe^0 increases with an increase of H^+, and H^+ is also involved in the reductive degradation of azo compounds (Guo et al. 2011). Thus, the initial pH may affect the performance of AO_7 removal by B-nZVI. Furthermore, a lower pH may help to avoid forming oxides which would reduce the activity of iron particles and then enhance the reductive degradation of AO_7 on the surface of nZVI particles.

3.2.2 Effect of the Dosage of B-nZVI on the Removal of AO_7

The influence of B-nZVI dosages on removal of AO_7 with 20 mg/L concentration at pH 7.0 was also investigated, and the results are illustrated in Fig. 6. As shown in Fig. 6a, the removal efficiencies within 10 min increased from 28.9 to 95.2 % with B-nZVI dosages increasing from 0.8 to 3.2 g/L. It was also observed that k_{obs} rose from 0.035 to 0.30 min^{-1} when the dosage of B-nZVI increased from 0.8 to 3.2 g/L (Fig. 6b), which is attributed to more active sites for AO_7 removal with an increase of B-nZVI dosages.

Figure 6c showed the relationship between k_{obs} and the dosage of B-nZVI with a good linearity (r^2=0.99), which was similar to other reports on nZVI application in wastewater treatment (Zhang et al. 2010). This again suggests that degradation of AO_7 by B-nZVI can be described by the pseudo-first-order kinetic model and the reduction process is mainly controlled by the active sites of B-nZVI.

3.3 Mechanism of AO_7 Degradation by B-nZVI

In order to reveal the potential degradation mechanism, the ultra-violet spectra of AO_7 solution in the range of 200–700 nm were recorded at reaction time (t) = 0, 5, and 30 min, respectively, and the results are shown in Fig. S3. Two typical peaks of AO_7 were observed at ~484 and ~305 nm corresponding to the absorption of the conjugated structure of azo benzene (Fig. S3a).

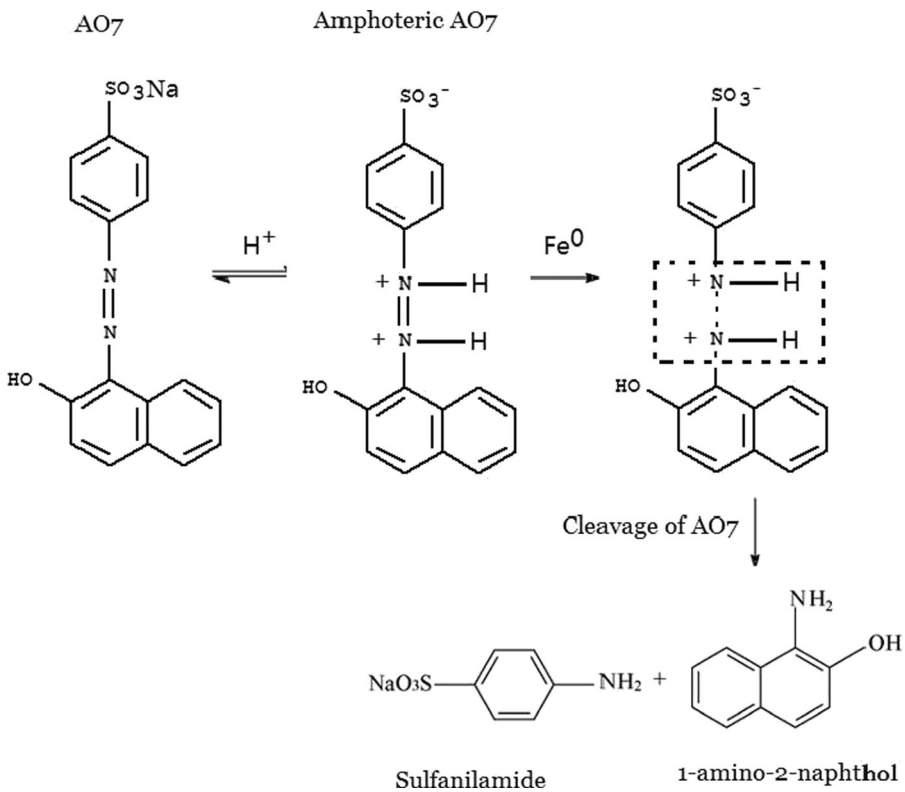

Scheme 1 Potential degradation pathway of AO_7 by B-nZVI

Under an acid condition, the amphoteric molecules may form because hydrogen ions would be attached to the nitrogen atoms of azo groups. During the reaction, azo groups were cleaved to two parts, and sulfanilamide and 1-amino-2-naphthol were probably the products (Liu et al. 2007). As shown in Fig. S3b (t=5 min), the peaks of ~484 and ~305 nm decreased quickly and disappeared after 30 min reaction (Fig. S3c), implying the complete destruction of AO_7. Meanwhile, the peak at ~254 nm became the strongest one, which was attributed to the absorption of soluble sulfanilamide molecules (Liu et al. 2007). As indicated by Kudlich et al. (1999), another final product, 1-amino-2-naphthol, could not be ascertained in ultra-violet spectra due to its auto-oxidation. The potential pathway for the reduction of AO_7 by B-nZVI was proposed in Scheme 1.

4 Conclusion

The B-nZVI was synthesized, characterized, and utilized for AO_7 removal. Kinetics analysis in batch studies demonstrated that the degradation of AO_7 by B-nZVI was controlled by active sites, and the data fit well with the pseudo-first-order equation. The initial pH was found to be an important factor in the degradation of AO_7 by B-nZVI. The reaction rate constant (k_{obs}) increased with the increase of B-nZVI dosage. At pH 7.0 and the dosage of B-nZVI 3.2 g/L, the removal of AO_7 was up to 95.2 % within 10 min. Therefore, it is concluded that B-nZVI has the potential to be a promising material for the degradation of organic contaminants.

Acknowledgments The project was financially supported by the National Natural Science Foundation of China (Grant No. 21377056) and by research fund of Key Laboratory for Advanced Technology in Environmental Protection of Jiangsu Province (Grant No. AE201319).

References

Azam, A., & Hamid, A. (2006). Effects of gap size and UV dosage on decolorization of C.I. Acid orange 7 by UV/H_2O_2 process. *Journal of Hazardous Materials, 133*, 167–171.

Brown, D. (1987). Effects of colorants in the aquatic environment. *Chemosphere, 12*, 397–404.

Cao, X., Ro, K. S., Libra, J., Kammnann, C., Lima, I., Berge, N., Li, L., Li, Y., Chen, N., Yang, J., Deng, B., & Mao, J.-D. (2013). Effects of biomass types and carbonization conditions on the chemical characteristics of hydrochars. *Journal of Agricultural and Food Chemistry, 61*, 9401–9411.

Chen, H., Zhao, Y. G., & Wang, A. Q. (2007). Removal of Cu(II) from aqueous solution by adsorption onto acid-activated palygorskite. *Journal of Hazardous Materials, 149*, 346–354.

Chen, B., Chen, Z., & Lu, S. (2011). A novel magnetic biochar efficiently sorbs organic pollutants and phosphate. *Bioresource Technology, 102*, 716–723.

Forgacs, E., Cserháti, T., & Oros, G. (2004). Removal of synthetic dyes from wastewaters: a review. *Environmental International, 30*, 953–971.

Guo, J., Jiang, D., Wu, Y., Zhou, P., & Lan, Y. (2011). Degradation of methyl orange by Zn(0) assisted with silica gel. *Journal of Hazardous Materials, 194*, 290–296.

Han, F., Kambala, V. S. R., Srinivasan, M., Rajarathnam, D., & Naidu, R. (2009). Tailored titanium dioxide photocatalysts for the degradation of organic dyes in wastewater treatment: a review. *Applied Catalysis A, 359*, 25–40.

He, F., & Zhao, D. (2005). Preparation and characterization of a new class of starch-stabilized bimetallic nanoparticles for degradation of chlorinated hydrocarbons in water. *Environmental Science & Technology, 39*, 3314–3320.

Hoch, L. B., Mack, E. J., Hydutsky, B. W., Hershman, J. M., Skluzacek, J. M., & Mallouk, T. E. (2008). Carbothermal synthesis of carbon-supported nanoscale zero-valent iron particles for the remediation of hexavalent chromium. *Environmental Science & Technology, 42*, 2600–2605.

Huang, C. P., Wang, H. W., & Chiu, P. C. (1998). Nitrate reduction by metallic iron. *Water Research, 32*, 2257–2264.

Kudlich, M., Hetheridge, M. J., Knackmuss, H. J., & Stolz, A. (1999). Autoxidation reactions of different aromatic o-aminohydroxynaphthalenes that are formed during the anaerobic reduction of sulfonated azo dyes. *Environmental Science & Technology, 33*, 896–901.

Liu, H., Li, G., Qu, J., & Liu, H. (2007). Degradation of azo dye acid orange 7 in water by Fe^0/granular activated carbon system in the presence of ultrasound. *Journal of Hazardous Materials, 144*, 180–186.

Liu, T., Zhao, L., Sun, D., & Tan, X. (2010). Entrapment of nanoscale zero-valent iron in chitosan beads for hexavalent chromium removal from wastewater. *Journal of Hazardous Materials, 184*, 724–730.

Luo, S., Qin, P. F., Shao, J. H., Peng, L., Zeng, Q. R., & Gu, J. D. (2013). Synthesis of reactive nanoscale zero valent iron using rectorite supports and its application for orange II removal. *Chemical Engineering Journal, 223*, 1–7.

Malik, P. K., & Saha, S. K. (2003). Oxidation of direct dyes with hydrogen peroxide using ferrous ion as catalyst. *Separation Science and Technology, 31*, 241–250.

Martínez-Huitle, C. A., & Brillas, E. (2009). Decontamination of wastewaters containing synthetic organic dyes by electrochemical methods: a general review. *Applied Catalysis B, 87*, 105–145.

Nam, S., & Tratnyek, P. G. (2000). Reduction of azo dyes with zero-valent iron. *Water Research, 34*, 1837–1845.

Park, H., & Choi, W. (2003). Visible light and Fe(III)-mediated degradation of acid orange 7 in the absence of H_2O_2. *Journal of Photochemistry and Photobiology A, 159*, 241–247.

Phenrat, T., Saleh, N., Sirk, K., Tilton, R. D., & Lowry, G. V. (2007). Aggregation and sedimentation of aqueous nanoscale zerovalent iron dispersions. *Environmental Science & Technology, 41*, 284–290.

Quan, G., Zhang, J., Guo, J., & Lan, Y. (2014). Removal of Cr(VI) from aqueous solution by nanoscale zero valent iron grafted on acid-activated attapulgite. *Water, Air, and Soil Pollution, 225*, 1979.

Shi, L. N., Zhang, X., & Chen, Z. L. (2011). Removal of chromium (VI) from wastewater using bentonite-supported nanoscale zero-valent iron. *Water Research, 45*, 886–892.

Szpyrkowicz, L., Juzzolino, C., & Kaul, S. N. (2001). A comparative study on oxidation of disperse dyes by electrochemical process, ozone, hypochlorite and Fenton reagent. *Water Research, 35*, 2129–2136.

Wang, C. B., & Zhang, W. X. (1997). Synthesizing nanoscale iron particles for rapid and complete dechlorination of TCE and PCBs. *Environmental Science & Technology, 31*, 2154–2156.

Wang, A., Guo, W., Hao, F., Yue, X., & Leng, Y. (2014). Degradation of acid orange 7 in aqueous solution by zero-valent aluminum under ultrasonic irradiation. *Ultrasonics Sonochemistry, 21*, 572–575.

Xu, G., Sun, J., Shao, H., & Chang, S. X. (2014). Biochar had effects on phosphorus sorption and desorption in three soils with differing acidity. *Ecological Engineering, 62*, 54–60.

Yao, Y., Gao, B., Inyang, M., Zimmerman, A. R., Cao, X., Pullammanappallil, P., & Yang, L. (2011). Biochar derived from anaerobically digested sugar beet tailings: characterization and phosphate removal potential. *Bioresource Technology, 102*, 6273–6278.

Yao, Y., Gao, B., Chen, J., Zhang, M., Li, M. I. Y., Alva, A., & Yang, L. (2013). Engineered carbon (biochar) prepared by direct pyrolysis of Mg-accumulated tomato tissues: characterization and phosphate removal potential. *Bioresource Technology, 138*, 8–13.

Zhang, J. H., Hao, Z. W., Zhang, Z., Yang, Y. P., & Xu, X. H. (2010). Kinetics of nitrate reductive denitrification by nanoscale zero-valent iron. *Process Safety and Environment Protection, 88*, 439–445.

Zhang, M., Gao, B., Yao, Y., Xue, Y., & Inyang, M. (2012). Synthesis of porous MgO-biochar nanocomposites for removal of phosphate and nitrate from aqueous solutions. *Chemical Engineering Journal, 210*, 26–32.

Zhou, Y., Gao, B., Zimmerman, A. R., Chen, H., Zhang, M., & Cao, X. (2014). Biochar-supported zerovalent iron for removal of various contaminants from aqueous solutions. *Bioresource Technology, 152*, 538–542.